J Mater Sci: Mater Electron (2025) 36:2254

Structural, morphological, optical, and electrical properties of Sb_xSe_y films with different compositions grown by Chemical-molecular beam deposition method from Separate Sb and Se precursors

T. M. Razykov[1], K. M. Kouchkarov[1], B. A. Ergashev[1], R. R. Khurramov[1,*], D. Z. Isakov[1], and M. S. Tivanov[2]

[1] *Physical-Technical Institute, Chingiz Aytmatov Street 2B, 100084 Tashkent, Uzbekistan*
[2] *Faculty of Physics, Belarusian State University, Nezavisimosti Ave. 4, 220030 Minsk, Belarus*

Received: 25 July 2025
Accepted: 22 November 2025

ABSTRACT

Sb_xSe_y thin films were obtained by chemical-molecular beam deposition (CMBD) on soda–limeglass from high-purity Sb and Se precursors at 450 °C substrate temperature. By the exact control of separate sources temperature, Sb_xSe_y thin films with stoichiometric and different compositions were successfully obtained. The Sb_xSe_y thin films were characterized in terms of their elemental and phase composition, along with their crystal structure, using techniques such as energy-dispersive X-ray microanalysis, X-ray diffraction, Raman spectroscopy, scanning electron microscopy, and atomic force microscopy. The bandgap of the films, ranging between 1.07 and 1.26 eV, was determined by analyzing absorption spectra derived from transmittance and reflectance measurements using a spectrophotometer. The electrical properties of samples were measured by the two-probe method. The samples showed p-type conductivity at $Sb/Se \le 0.77$ and n-type conductivity at $Sb/Se \ge 0.95$. From this behavior, we infer the presence of a "turning point" at $Sb/Se = 0.77$, which corresponds to the p-type conductivity of Sb_2Se_3 thin films.

1 Introduction

Structural and morphological properties of antimony selenide thin films are one of the key factors governing the device performance of antimony selenide (Sb_2Se_3)-based thin-film solar cells. Thus, the controlling of structural and morphological parameters and obtaining stoichiometric composition plays an essential role [1–3]. In particular, the structural and morphological properties such as crystallographic orientation, grain size, and compactness play a crucial role in carrier transport, recombination, and overall

Address correspondence to E-mail: rkhurramov@yahoo.com

https://doi.org/10.1007/s10854-025-16307-4
Published online: 10 December 2025

device performance. Achieving highly oriented, large-grained, and stoichiometric Sb_2Se_3 films is therefore vital for enhancing photovoltaic performance [4].

To date, number of deposition technics were implemented to obtain Sb_2Se_3 thin films, such as vapor transport deposition [5], close-spaced sublimation [6], injection vapor deposition [7], magnetron sputtering [8], and pulsed laser deposition [9]. However, the selenium loss and re-evaporation of antimony selenide are inevitable [10] and it influences on properties of Sb_2Se_3 films. These issues severely deteriorate the optoelectronic quality of the films, thereby reducing device efficiency.

In order to suppress these phenomena, Sb_2Se_3 thin films were deposited from separate antimony and selenium sources at substrate temperatures of 450 °C. The controlling of selenium content during the deposition process was carried out by changing temperature of selenium source from 410 °C to 450 °C, whereas 900 °C was maintained at antimony source. This approach enables compensation for selenium loss during film growth, which has not been systematically addressed in our earlier studies [11, 12]. This study, therefore, offers both a novel processing strategy and a deeper physical understanding of how precise selenium control can promote high-quality Sb_2Se_3 film growth and affect morphological, structural, optical, and electrical properties of thin films.

2 Experiments

2.1 Synthesis of Sb_2Se_3

Sb_xSe_y thin films deposited from separate high purity of 99.999% Sb and Se granules. The temperature of Sb was maintained at 900 °C. The controlling of Se content during the deposition process was carried out by changing temperature of selenium source. 20 mm × 20 mm in size soda–lime glass (SLG) was used as a substrate. The SLG substrates were cleaned with detergent, acetone, ethanol, and deionized water in an ultrasonic bath and finally dried with a stream of N_2 gas. Sb_xSe_y thin films with a substrate temperature of 450 °C were obtained at atmospheric pressure with gaseous hydrogen at a flow rate of 20 cm^3/min in 30 min of evaporation time by chemical-molecular beam deposition which was further detailed in our previous work [11, 12]. The thin films had an average thickness of 2 μm, which was measured using a MIM-7 (POCC) metallographic vertical microscope.

2.2 Films characterization

To investigate the influence of varying Sb/Se ratios on the structural, morphological, optical, and electrical properties of Sb_xSe_y thin films, multiple analytical techniques were employed.

Surface morphology and topology were analyzed using a Carl Zeiss LEO-1455 VP scanning electron microscope (SEM) with 20 kV image operating voltage and a SOLVER NANO atomic force microscope (AFM), employing semi-contact mode scanning with a probe featuring a tip radius of 10 nm at a resonant frequency of 178 kHz. Chemical composition analysis was carried out via energy-dispersive X-ray spectroscopy (EDX) using an Oxford Instruments Aztec Energy Advanced X-Max 80 spectrometer with an accelerating voltage of 20 kV and an estimated penetration depth of about 1.6 microns. The crystalline structure was examined using a Rigaku Ultima IV X-ray diffractometer in grazing incidence diffraction (GIXD) mode, with an incident angle of 1° and a CuKα radiation source (λ = 1.54178 Å). Phase identification was conducted by comparing the obtained diffraction patterns with reference data from the Joint Committee on Powder Diffraction Standards (JCPDS) and the Crystallography Open Database. Raman spectroscopy measurements were performed at room temperature using a LOTIS TII Nanofinder HE confocal spectrometer. A 532 nm solid-state laser was used for excitation, with the power kept at 60 μW to prevent thermal degradation of the samples. The spectrometer achieved a spectral resolution better than 2.5 cm^{-1}, and the laser spot size on the sample surface was approximately 0.7 μm in diameter. Reflection and transmission measurements were carried out using a scanning spectrophotometer, namely, the PHOTON RT model by Essent Optics. The incident optical beam directed onto the sample surface measured approximately 2 × 6 mm^2. Electrical properties of samples were measured by two-probe method and the dependence of conductivity on temperature. The dependence of electrical conductivity on temperature was measured in the range from 270 to 110 K, while the pressure inside the cryostat varied between 5 and 1 Pa. The type of conductivity of the films was determined by thermo-probe method. These experimental techniques were employed to examine Sb_xSe_y thin films, with particular focus on how variations in

the Sb-to-Se ratio affect their crystalline structure, surface morphology, optical, and electrical characteristics.

3 Results and discussion

The results of energy dispersion analysis showed that the Sb_xSe_y films deposited from separate sources of Sb and Se at a substrate temperature of 450 °C have different compositions Sb/Se = 0.66, 0.72, 0.77, 0.95, 1.1, 1.26 for different temperatures of selenium source in the range of 410 ° C—450 °C.

Table 1 shows the EDS results of Sb_xSe_y thin films deposited with different temperatures of selenium source. From Table 1, it is clearly visible that the chemical composition was changed toward stoichiometric ratio of Sb/Se = 0.66 when selenium temperature was increased. As seen in Fig. 1, the distribution of the Sb and Se elements on the surfaces is almost uniform. The appearance of silicon, sodium, and oxygen peaks in the EDX spectrum can be explained by the elements detection from the SLG substrates and the oxygen adsorption from the atmosphere [13].

The influence of chemical composition changes on morphological properties of Sb_2Se_3 thin films can be seen from Fig. 2. As depicted in SEM images, the Sb_xSe_y films shows different morphologies with evolution of the composition. For the film with Sb/Se = 1.26, the non-uniform distribution of grains with different sizes can be seen, which can be attributed to selenium-poor composition in the film. The maximum grain size for this film was around 6 μm. For Sb/Se = 1.1, the identical distribution of grains was observed.

It can be seen that the film with atomic ratio of Sb/Se = 0.95 has similar morphology like Sb/Se = 1.1 but scattered grains on the surface of the Sb/Se = 0.95. Films with atomic ratio of Sb/Se = 0.77 has uniform distribution of grains as compared to that of Sb/Se = 0.95 and still scattered grains on the surface of the film. When the atomic ratio was 0.77, the sample showed

Table 1 EDS results for Sb_xSe_y thin films

№	1	2	3	4	5	6
Sb	55.9	52.2	48.7	43.6	41.9	39.6
Se	44.1	47.8	51.3	56.4	58.1	60.4
Sb/Se	1.26	1.1	0.95	0.77	0.72	0.66

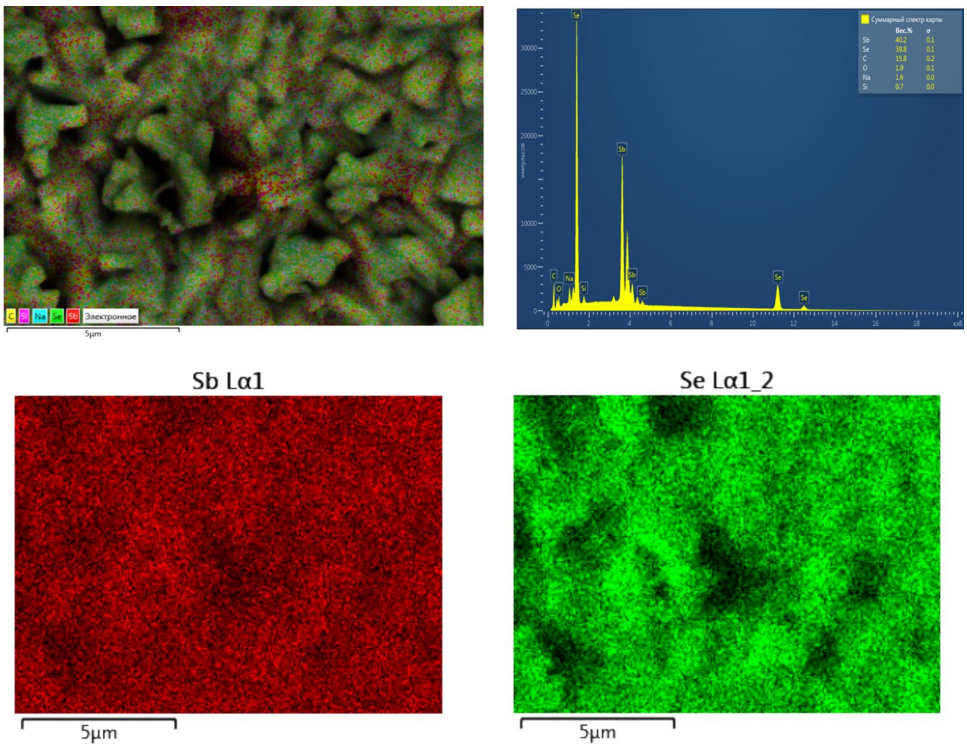

Fig. 1 EDS mapping images of Sb/Se = 0.66 sample

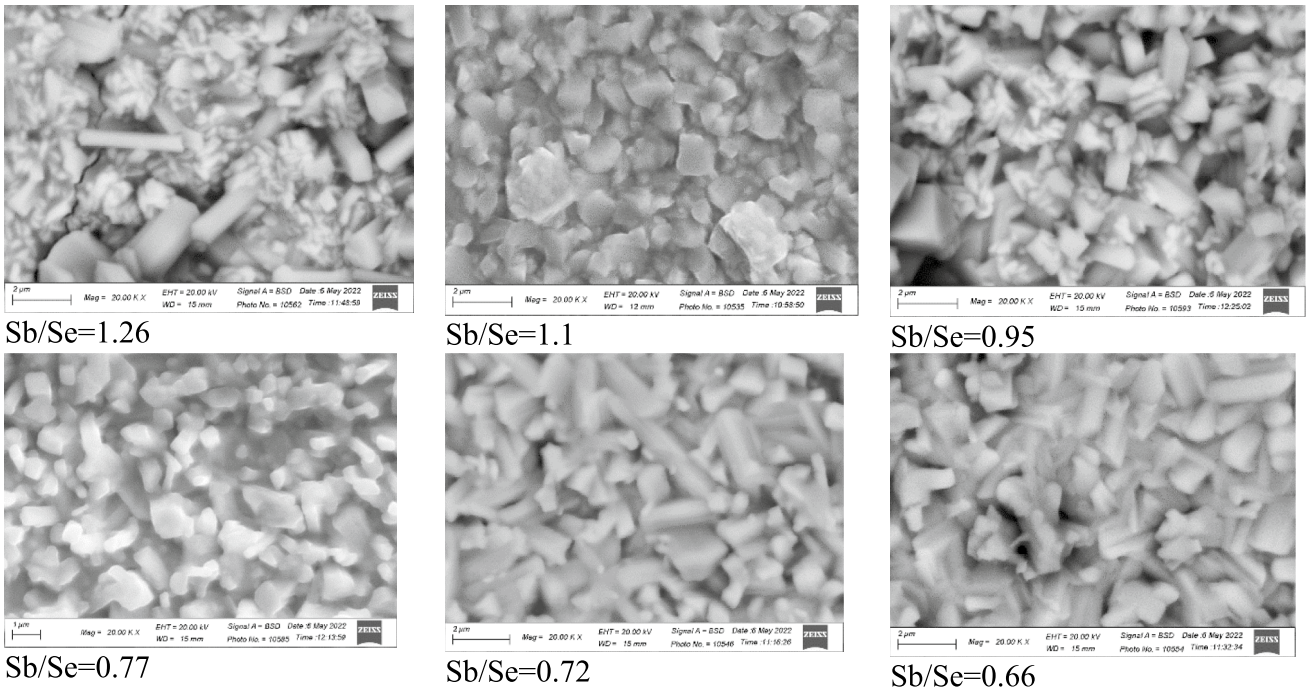

Fig. 2 SEM images of Sb_xSe_y thin films

dense and uniform distribution with 1–4-µm-rod-shaped grains. The subsequent increasing of selenium content in the time of deposition leads to the stoichiometric ratio 0.66 and the morphology was similar to the film with chemical composition 0.72.

For investigating more comprehensive of Sb_xSe_y thin films, AFM analysis was conducted (Table 2). The resulting surface parameters including average roughness (Sa), root mean square roughness (Sq), skewness (Ssk), and kurtosis (Ska) highlight the influence of chemical composition on the surface morphology of the films. Average Roughness (Sa) which measures the mean deviation of the surface profile from the average plane increases progressively with higher Sb content. The lowest Sa value of 0.21 µm was observed for the Sb/Se = 0.72 film, indicating a relatively smoother surface. In contrast, the film with Sb/Se = 1.26 exhibited the highest Sa of 0.76 µm, suggesting a rougher topography as the Sb concentration increases. Root Mean Square Roughness (Sq), which provides a more sensitive measure of surface roughness by emphasizing larger deviations, follows a similar trend. It ranged from 0.28 µm for Sb/Se = 0.72 to 0.95 µm for Sb/Se = 1.26, reinforcing the observation that increasing Sb content leads to rougher surfaces. The surface roughness of samples decreased on higher Se concentration leads to a significant improvement to the surface quality [14]. The skewness (Ssk) values, which describe the asymmetry of surface height distribution, remained positive across all compositions. This suggests a predominance of peaks over valleys on the surface. The kurtosis (Ska) values, which reflect the sharpness or flatness of the surface profile, varied between 3.13 and 4.48. The highest Ska value was recorded for Sb/Se = 0.72, suggesting a surface dominated by sharp features or spikes. Other compositions showed kurtosis values around or just above 3, indicating

Table 2 AFM data for Sb_xSe_y thin films with different compositions

Samples (Sb/Se)	0.66	0.72	0.77	0.95	1.1	1.26
Roughness average Sa, µm	0.33	0.21	0.37	0.42	0.56	0.76
Root Mean Square Roughness Sq, µm	0.41	0.28	0.48	0.54	0.73	0.95
Skewness Ssk	0.63	0.83	0.94	0.89	0.81	0.64
Kurtosis Ska	3.13	4.48	4.25	3.78	3.79	3.22

surfaces with near-Gaussian or slightly peaked height distributions (Table 2).

X-ray diffraction (XRD) analysis was performed to investigate the crystallographic structure and phase composition of the Sb_xSe_y thin films deposited at a substrate temperature of 450 °C. XRD is a powerful characterization technique based on the constructive interference of monochromatic X-rays and a crystalline sample. The positions (2θ) and intensities of the resulting diffraction peaks provide direct information about the crystal structure, lattice spacing, crystallite orientation, and degree of crystallinity of thin films. As discussed by H.H. Radamson [15], understanding the origin and interpretation of these diffraction patterns is essential for correlating structural properties with the physical performance of crystalline materials. Figure 3 depicts the XRD pattern for Sb_xSe_y thin films grown with different chemical compositions at 450 °C substrate temperature. Many peaks are observed in the range 2Θ from 15° to 60° to indicate the films' crystal structure. Two single peaks at 2Θ ≈ 15.05° and 2Θ ≈ 16.85° are associated with the (020) and (120) planes, single peak at 2Θ ≈ 28.25 ÷ 28.75 are associated with the (211) plane, peaks at 2Θ ≈ 31.20, at 2Θ ≈ 51.90 are associated with the (221) and (061) planes, group of peaks in the range of 2Θ = 45.00 ÷ 46.00 are associated with the (431), (501), (530), (151), and (002) planes, respectively, corresponding to the orthorhombic crystal lattice of Sb_2Se_3 described in the available database (JCPDS no. 00–015–0861). These peaks are observed at all diffraction patterns and defined as belonging to an orthorhombic crystal lattice of Sb_2Se_3. The parameters of the crystal lattice were determined as b≅ 11.764Å, c≅3.975Å using peaks of (020) and (002) planes by the Wolf-Bragg's formula

$$2d \sin\theta = n\lambda \tag{1}$$

where λ is incident CuKα radiation wavelength; θ is Bragg angle.

Lattice parameter a≅11.724 was calculated by the Lipson difference method

$$\frac{n^2}{d^2} = \frac{h^2}{a^2} + \frac{k^2}{b^2} + \frac{l^2}{c^2} = Q_{hkl} = \frac{4}{\lambda^2}\sin^2\theta_{hkl} \tag{2}$$

using peaks of (020) and (120) planes.

$$Q_{120} - Q_{020} = \frac{4}{\lambda^2}\left(\sin^2\theta_{120} - \sin^2\theta_{020}\right) = \frac{1}{a^2} \tag{3}$$

The results of calculation correlate with data in JCPDS 00–015–0861 card: a=11.633 Å, b=11.780 Å, c=3.985 Å From Fig. 3, it can be seen that the variation of the selenium content during deposition process has direct impact not only on chemical composition, but also on the structural properties of obtained films having favorable (*hkl*, $l = 1$) and/or unfavorable (*hkl*, $l = 0$) peaks. In particular, the occurrence of peaks along (*hkl*, $l = 1$) planes is considered favorable for vertical carrier transport, while (*hkl*, $l = 0$) orientations are known to hinder charge movement through the film bulk. For example, the samples with chemical compositions of 1.26, 1.1, 0.95 showed mainly.

(012), (104), (110) dominant peaks related to Sb according to (JCPDS#01–085–1322). Moreover, films with the Se-poor chemical composition (Sb/Se ≥ 0.95) have Sb_2Se_3 peaks such as (020), (120), (061), (211), and (221) according to (JCPDS#00–015–0861). A transition of the dominant peaks from Sb to Sb_xSe_y was observed depending on the Se concentration. For films Sb/Se = 1.1, Sb/Se = 0.95, and Sb/Se = 0.77, there were nearly identical results such as (020), (120), (130), and (211) peaks. As the subsequent increasing selenium content, the samples with Sb/Se = 0.72 and Sb/Se = 0.66 show (020), (120), and (061) peaks with higher intensities compared to other samples. It should be point out that with increasing the selenium concentration during deposition process, the intensities of all peaks such as (020), (120), (211), (221), (061) corresponding to Sb_2Se_3 are enhanced, which was also observed on Sb_2Se_3 film with stoichiometric composition of Sb/Se = 0.66. It is reasonable to assume that increasing selenium concentration promotes the formation and crystallinity of the orthorhombic Sb_2Se_3 phase, with a preferred orientation along (hk1) planes. Since carrier transport in Sb_2Se_3 is known to be more efficient along the (hk1) direction compared to the (hk0) orientation, which tends to block carrier flow, optimizing the Se content is essential for achieving better electronic properties in these films and solar cells based on them [16].

Microstructural parameters: the coherent scattering region size (L) and the lattice deformation (ε) were determined by using of the Williamson–Hall method, in which it is assumed that the broadening of the diffraction peak (β_{hkl}) is determined by the size (β_D) and strain (β_S) broadenings. In the uniform deformation model (UDM), the Williamson–Hall equation looks as follows [17]:

$$\beta \cdot \cos\theta = \frac{K\lambda}{L} + 4\varepsilon \cdot \sin\theta, \quad (4)$$

where K is shape factor (0.94), $\beta = \left(\frac{\pi}{4\ln 2}\right)^{\frac{1}{2}} \cdot FWHM$.

The dependence of $\beta\cos\theta$ on $4\sin\theta$ was drawn for the singular peaks observed at almost all diffraction patterns with crystallographic planes (020), (120), (230), (221), (240), (321) of the orthorhombic structure. The linear approximation of the obtained results allowed for determination of the values of the coherent scattering region and the lattice strain [18]. As was found from the graphical dependences, the value of the lattice deformation (ε) for all samples is of the order of zero ($<10^{-4}$) (for example, Fig. 4 shows a graphical construction for the case Sb/Se = 0.77). The values of the coherent scattering region (L) ranges from 27 to 44 nm.

Raman spectroscopy was employed to further examine the vibrational properties and phase evolution of the Sb_xSe_y thin films deposited at 450 °C. Raman scattering is a non-destructive technique that probes the inelastic scattering of monochromatic light by phonons in a material. The positions, shapes, and intensities of the Raman peaks provide direct information about the bonding structure, chemical composition, crystalline quality, and presence of secondary phases in nanomaterials. This makes Raman analysis particularly useful for distinguishing between different Sb–Se, Sb, and Se phases that may coexist during non-stoichiometric growth of Sb_xSe_y thin film.

The Raman spectra of Sb_xSe_y films as-deposited with various chemical composition are illustrated in Fig. 5. The phase transition dependence on chemical composition of samples is observed. It is noted that Sb–Se, Sb-O, Sb, and Se have the following peaks in Raman spectra: Sb_2O_4 – 72, 141, 198, 255, 400, 463 cm^{-1}; cubic Sb_2O_3 – 82, 189, 254, 373, 450 cm^{-1}; rhombohedral Se_6 – 67, 72, 102, 129, 221, 246 cm^{-1}; orthorhombic Sb_2Se_3 – 79, 120, 151, 189, and 210 cm^{-1}; trigonal Se_n – 140, 234–237 cm^{-1}; -monoclinic Se_8 – 111, 252 cm^{-1}; and rhombohedral Sb – 109, 150 cm^{-1} [19]. It has been reported that peak positions at 188 cm^{-1} also belong to Sb_2Se_3 obtained via a simple PEG-400 polymer chain-assisted growth route in the temperature range of 160–180 °C [20]. For Se-poor condition, two antimony peaks at around 110 cm^{-1} and 150 cm^{-1} are reported [21], which is consistent with our thin films with atomic ratio of Sb/Se = 1.26 and Sb/Se = 1.1. In addition, intensities at 103 cm^{-1} and 153 cm^{-1} were detected in films deposited by a low-temperature vacuum evaporation process [22]. However, there is a peak at 189 cm^{-1} for the film with chemical composition Sb/Se = 1.1 corresponding to Sb_2Se_3 as a result of the increase of Se in the film composition as compared to the film with Sb/Se = 1.26. In the literature, the peaks at 190 cm^{-1} and 210 cm^{-1} are usually caused by Sb–Se vibration mode [20, 23–25]. As the chemical composition changes to Sb/Se = 0.95, together with the appearance of the 189 cm^{-1}, others peaks are detected at 102 cm^{-1} and 210 cm^{-1}, which is assigned to rhombohedral selenium and Sb_2Se_3, respectively [20]. The peak at about 103 cm^{-1} is assigned to Se_6 ring of rhombohedral Se [21]. Due to the subsequent changing of chemical composition from Sb/Se = 0.95 to Sb/Se = 0.72, there are peaks at 67–72 cm^{-1}, 102 cm^{-1}, 151 cm^{-1}, 190 cm^{-1}, 210 cm^{-1}. It should be noted that the intensities at 67–72 cm^{-1} and 210 cm^{-1} are also observed in the composition of 0.95 and 1.1. When the atomic ratio changes to Sb/Se = 0.66, the sample shows a dominant intensity at 189 cm^{-1} with less intensities at 67–72 cm^{-1}, 102 cm^{-1}, 151 cm^{-1}, 210 cm^{-1}. Overall, the Raman spectra showed that the film deposited at 450 °C of the substrate temperature has peaks at 110 cm^{-1} and 150 cm^{-1}, which are related to rhombohedral antimony under Se-poor condition. When Se increases in the film composition, there are detected decreasing of antimony intensities and antimony selenide phases emerged at 189 cm^{-1}, 210 cm^{-1} under Se-rich condition during deposition process suggesting good film quality.

The bandgap of a semiconductor material is one of the crucial part characteristic, which can be obtained by measuring the optical specular reflectance and transmittance of the films (Fig. 6ab). The absorption coefficient (α) of all Sb_xSe_y thin films deposited at various Sb/Se ratios was converted from transmission (T) and reflection (R) spectral data in 400–3000 nm spectral region with the following equation [26]:

$$\alpha = \left(-\frac{1}{d}\right) \ln\left(\frac{\sqrt{(1-R)^4 + 4T^2R^2} - (1-R)^2}{2TR^2}\right), \quad (5)$$

Table 3 Electrical properties of Sb_xSe_y thin films with different compositions

Sb/Se	0.66	0.72	0.77	0.95	1.1	1.26
Conductivity type	p	p	p	n	n	n
Electroconductivity $(\Omega\ cm)^{-1}$	$3.45\ 10^{-5}$	$3.06\ 10^{-5}$	$6.6\ 10^{-6}$	$3.9\ 10^{-1}$	$1.87\ 10^{1}$	$4.7\ 10^{2}$
Activation energy (meV)	140	151	220	32	29	Not defined

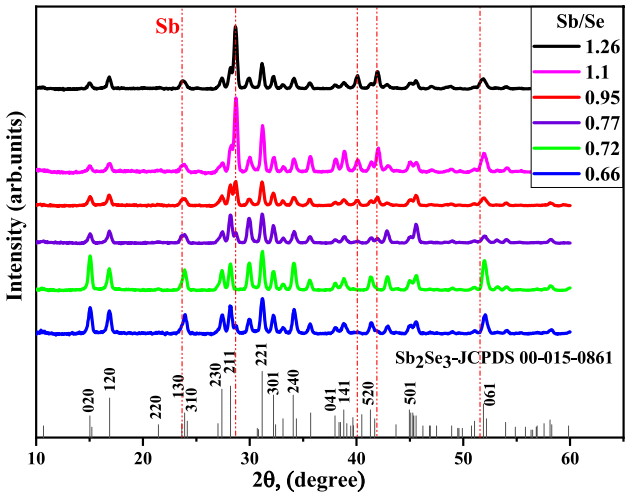

Fig. 3 The XRD data of Sb_xSe_y thin films with different chemical compositions

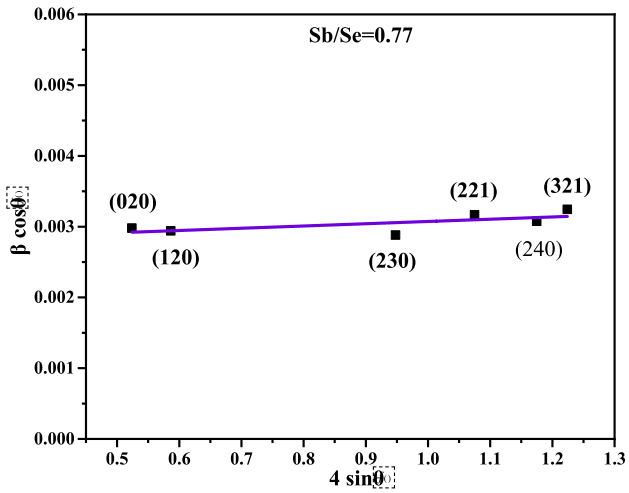

Fig. 4 Williamson–Hall plots of Sb_2Se_3 thin film for Sb/Se = 0.77

$$\alpha = \left(-\frac{1}{d}\right)\ln\left(\frac{\sqrt{(1-R)^4 + 4T^2R^2} - (1-R)^2}{2TR^2}\right), \quad (5)$$

There d- thickness of the films.

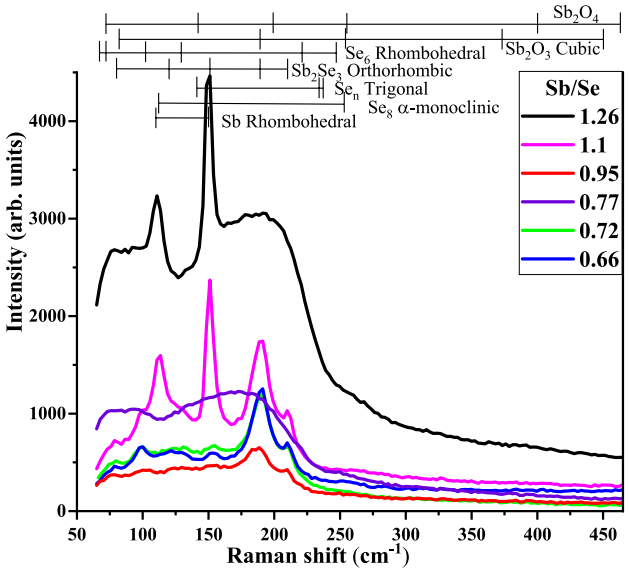

Fig. 5 Raman spectra of Sb_xSe_y thin films with various chemical composition

The optical bandgap of the films was calculated using the Tauc equation [27] for direct bandgap semiconductors:

$$(\alpha h\nu)^2 = A\left(h\nu - E_g\right), \quad (6)$$

where $h\nu$ is the photon energy and A is a constant dependent on the effective mass. Figure 6c presents the Tauc plots for the Sb_xSe_y thin films, revealing bandgap values between 1.07 and 1.26 eV. The highest bandgap corresponds to the stoichiometric ratio, while the lowest occurs in antimony-rich compositions (Sb/Se = 0.95). Compared to pure Sb_2Se_3 (bandgap ~ 1.15 eV) [28], the Sb_xSe_y films exhibit a slight variation in bandgap, likely due to structural changes from disordered to ordered atomic arrangements and absorption at rhombohedral Se. These findings align with prior studies, confirming that the optical and structural properties of Sb_xSe_y films strongly depend on the Sb/Se ratio [29].

The electrical conductivity of Sb_2Se_3 thin films enriched with antimony and close to stoichiometric

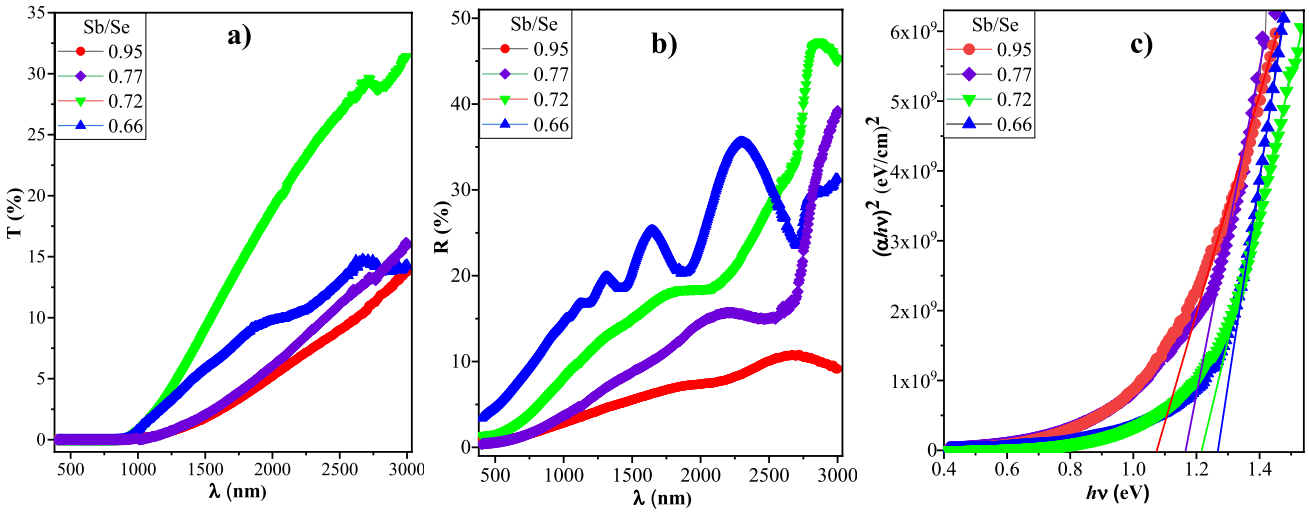

Fig. 6 **a** Transmission; **b** Reflection spectra; and **c** Tauc plots of Sb_xSe_y thin films deposited at different Sb/Se ratios

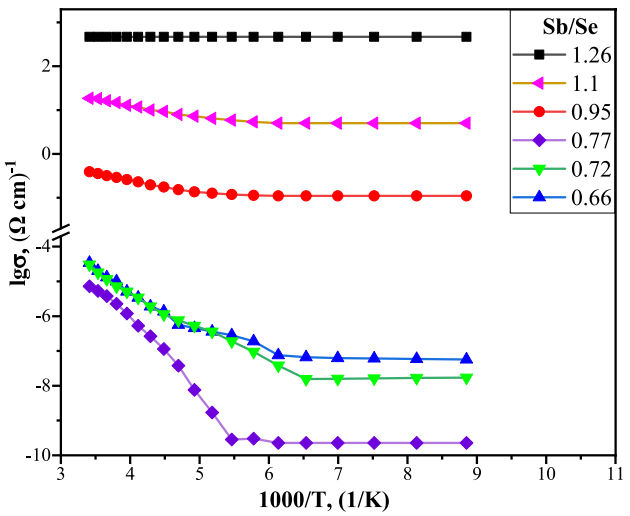

Fig. 7 Arrhenius plots of Sb_xSe_y thin films

composition was determined using the temperature dependence of conductivity based on the Arrhenius equation:

$$\sigma = \sigma_0 \exp\left(-\frac{E_a}{kT}\right) \quad (7)$$

where σ is the specific conductivity in the dark, σ_0 is a pre-exponential factor, E_a is the activation energy for conductivity, k is the Boltzmann constant, and T is the absolute temperature.

Figure 7 presents the Arrhenius plots for Sb_xSe_y thin films grown at a substrate temperature of 450 °C with varying Sb/Se ratios. As evident from the graph, within the Sb/Se range of $0.95 \le Sb/Se \le 1.26$, the electrical conductivity of the Sb_xSe_y thin films varied within a narrow range. A change in the conductivity type of charge carriers was also observed depending on the Sb/Se atomic concentration ratio. The samples exhibited n-type conductivity within the compositional range $0.95 \le Sb/Se \le 1.26$ and p-type conductivity in the range $0.66 \le Sb/Se \le 0.77$. Notably, a conductivity-type inversion was observed at Sb/Se = 0.77, which corresponds to a composition close to stoichiometric Sb_2Se_3.

The specific conductivity of Sb_xSe_y thin films is highly dependent on the Sb/Se ratio. Figure 7 shows the dependence of sample conductivity on the Sb/Se ratio. It can be seen that in thin films.

with Sb/Se ratios in the range $0.66 \le Sb/Se \le 0.77$, the conductivity values vary around 10^{-5} $(\Omega \cdot cm)^{-1}$. The slight decrease in electrical conductivity observed with increasing Sb content in the p-type samples can be attributed to the reduced concentration of acceptor energy levels associated with defect states such as antimony vacancies (V_{Sb}) and antisite defects (Se_{Sb}). At Sb/Se = 0.95, the conductivity increases sharply from 10^{-5} $(\Omega \cdot cm)^{-1}$ to 10^{-1} $(\Omega \cdot cm)^{-1}$, and continues to increase steadily up to Sb/Se = 1.26, reaching approximately 2.5×10^2 $(\Omega \cdot cm)^{-1}$. Furthermore, we established that the type of charge carriers undergoes conversion depending on the Sb/Se ratio. The samples showed p-type conductivity at $Sb/Se \le 0.77$ and n-type conductivity at $Sb/Se \ge 0.95$. From this behavior, we infer the presence of a

"turning point" at Sb/Se = 0.77, which corresponds to the p-type conductivity of Sb_2Se_3 thin films (Table3).

The activation energy was derived from the temperature dependence of the electrical conductivity of Sb_xSe_y thin films with varying compositions. The activation energy was determined at T > 180 K, since the region of lower temperatures corresponded to the "freeze-out" regime (Fig. 7). The purpose of determining the activation energy was to identify the types of defects present in the Sb_xSe_y thin films, as certain defects in Sb_2Se_3 thin films can lead to a reduced open-circuit voltage. According to the literature, the dominant acceptor defects in Sb_2Se_3 thin films are V_{Sb} and Se_{Sb}, while the donor defects include V_{Se1}, V_{Se2}, V_{Se3}, Sb_{Se1}, Sb_{Se2}, and Sb_{Se3} [29, 30]. For thin films with Sb/Se = 0.95 and 1.1 ratios, the activation energy was approximately 30 meV. For thin films with Sb/Se = 1.26 ratio, the value of the activation energy cannot be determined due to the lack of a slope for the temperature dependence of electrical conductivity. This is probably due to the noticeable manifestation of the metallic conductivity mechanism due to the high antimony content. In films with excess antimony, selenium vacancies (V_{Se}) and antisite defects (Sb_{Se}) are likely dominant. For thin films with Sb/Se ratios from 0.77 up to stoichiometric composition, the activation energy varied from 0.14 eV to 0.22 eV. Activation energies in the range $E_a = 0.14 \div 0.22$ eV, as reported in the literature [31], correspond to acceptor defects such as V_{Sb1}, V_{Sb2}, and Se_{Sb2}, as well as donor defects such as V_{Se2} and Sb_{Se1}. For films close to the stoichiometric composition, the dominant defects are considered to be V_{Sb1} and Se_{Sb2}.

4 Conclusion

This study systematically investigated the synthesis, structural, morphological, optical, and electrical properties of Sb_xSe_y thin films deposited via chemical-molecular beam deposition at a substrate temperature of 450 °C with varying Sb/Se ratios. The results demonstrated that the chemical composition significantly influenced the structural, morphological, optical, and electrical properties of the films. EDS analysis confirmed a shift toward stoichiometric Sb_2Se_3 (Sb/Se = 0.66) with increasing selenium content. SEM and AFM revealed that films with higher Sb content (Sb/Se ≥ 0.95) exhibited non-uniform grain distribution and increased surface roughness, while films closer to stoichiometry showed denser and more uniform morphologies. XRD and Raman spectroscopy confirmed the presence of orthorhombic Sb_2Se_3 phases, with peak intensities enhancing as selenium content increased. The intensity of preferred (hk1) orientations increased with higher selenium content, suggesting improved crystallinity for stoichiometric compositions.

Optical analysis revealed bandgap values between 1.07 and 1.26 eV, with the highest bandgap corresponding to the stoichiometric ratio. Electrical measurements indicated a transition from p-type to n-type conductivity at Sb/Se = 0.77, with conductivity increasing sharply in Sb-rich compositions. Activation energy analysis suggested the dominance of selenium vacancies (V_{Se}) and antisite defects (Sb_{Se}) in Sb-rich films, while acceptor defects like V_{Sb} and Se_{Sb} were prominent near stoichiometry. These findings highlight the critical role of composition in tailoring the properties of Sb_xSe_y thin films for optoelectronic applications, providing valuable insights for optimizing their performance in devices such as solar cells and sensors.

Author contributions

All authors contributed to the research conception and design manuscript. Material preparation, data collection, and analysis were performed by Khurramov Ramozan Ravshanovich, Kudrat Mamarasulovich Kuchkarov, Mikhail Sergeevich Tivanov, and Takhir Mutalovich Razykov; Conceptualization: Takhir Mutalovich Razykov, Khurramov Ramozan Ravshanovich, Mikhail Sergeevich Tivanov, and Kudrat Mamarasulovich Kuchkarov; Methodology: Takhir Mutalovich Razykov, Khurramov Ramozan Ravshanovich, and Mikhail Sergeevich Tivanov; Formal analysis and investigation: Takhir Mutalovich Razykov, Khurramov Ramozan Ravshanovich, Ergashev Bobur, and Isakov Diyorbek; Thin film deposition: Khurramov Ramozan Ravshanovich and Isakov Diyorbek; Writing—original draft preparation: Takhir Mutalovich Razykov, and Khurramov Ramozan Ravshanovich; Funding acquisition: Takhir Mutalovich Razykov, Kudrat Mamarasulovich Kuchkarov, Mikhail Sergeevich Tivanov, and Khurramov Ramozan Ravshanovich; Resources: Kudrat Mamarasulovich Kuchkarov, Mikhail Sergeevich Tivanov, and Khurramov Ramozan Ravshanovich; Supervision: Takhir Mutalovich Razykov and Mikhail Sergeevich

Tivanov; All authors read and approved the final manuscript.

Funding

This work was supported by the basic research program of the Academy of Sciences of the Republic of Uzbekistan and the Belarusian Republican Foundation for Fundamental Research (Grant No: F25UZBG-109).

Data availability

The data used in the current study are available from the corresponding author on reasonable request.

Declarations

Conflict of interest There are no conflicts of interest to disclose between the authors.

References

1 G.X. Liang, Y. Di Luo, S. Chen, R. Tang, Z.H. Zheng, X.J. Li, X.S. Liu, Y.K. Liu, Y.F. Li, X.Y. Chen, Z.H. Su, X.H. Zhang, H.L. Ma, P. Fan, Sputtered and selenized Sb_2Se_3 thin-film solar cells with open-circuit voltage exceeding 500 mV. Nano Energy **73**, 104806 (2020). https://doi.org/10.1016/J.NANOEN.2020.104806

2 Y. Zhao, Sh. Wang, Ch. Li, B. Che, X. Chen, H. Chen, R. Tang, X. Wang, G. Chen, T. Wang, J. Gong, T. Chen, X. Xiao, J. Li, Regulating deposition kinetics via a novel additive-assisted chemical bath deposition technology enables 10.57%-efficient Sb_2Se_3 solar cells. Energy Environ. Sci. (2022). https://doi.org/10.1039/D2EE02261C

3 X. Liang, X. Wang, Q. Chang, B. Yang, W. Dang, Z. Zhang, Y. Guo, L. Yang, Z. Li, Reduction of bulk and interface defects via photo-annealing treatment for high-efficiency antimony selenide solar cells. Energy Environ. Sci. (2024). https://doi.org/10.1039/d4ee02877e

4 Sh. Zhang, Ch. Wu, J. Zeng, X. Meng, R. Hu, J. Wang, K. Chen, Grain size and absorber thickness than solely controlling orientation for fabricating high-performance Sb_2Se_3 solar cells. J. Phys. Chem. Lett. **16**, 8928–8935 (2025). https://doi.org/10.1021/acs.jpclett.5c02137

5 X. Wen, C. Chen, S. Lu, K. Li, R. Kondrotas, Y. Zhao, W. Chen, L. Gao, C. Wang, J. Zhang, G. Niu, J. Tang, Vapor transport deposition of antimony selenide thin film solar cells with 7.6% efficiency. Nat. Commun. (2018). https://doi.org/10.1038/s41467-018-04634-6

6 Z. Li, X. Liang, G. Li, H. Liu, H. Zhang, J. Guo, J. Chen, K. Shen, X. San, W. Yu, R.E.I. Schropp, Y. Mai, 9.2%-efficient core-shell structured antimony selenide nanorod array solar cells. Nat. Commun. (2019). https://doi.org/10.1038/s41467-018-07903-6

7 A. Mo, B. Yang, X. Lu, Y. Duan, X. Liang, Z. Zhang, Y. Guo, Z. Li, Reducing parasitic loss and deep defect formation via copper doping toward highly efficient Sb_2Se_3 solar cells. Adv. Funct. Mater. **2420261**, 1–12 (2025). https://doi.org/10.1002/adfm.202420261

8 Sh. Chen, Z. Zheng, M. Cathelinaud, H. Ma, X. Qiao, Z. Su, P. Fan, G. Liang, X. Fan, X. Zhang, Magnetron sputtered Sb_2Se_3-based thin films towards high performance quasi-homojunction thin film solar cells. Sol. Energy Mater. Sol. Cells **203**, 110154 (2019). https://doi.org/10.1016/j.solmat.2019.110154

9 K. Yang, B. Li, G. Zeng, Sb_2Se_3 thin film solar cells prepared by pulsed laser deposition. J. Alloy. Compd. **821**, 153505 (2020). https://doi.org/10.1016/j.jallcom.2019.153505

10 K. Yang, B. Li, G. Zeng, Effects of substrate temperature and SnO_2 high resistive layer on Sb_2Se_3 thin film solar cells prepared by pulsed laser deposition. Sol. Energy Mater. Sol. Cells **208**, 110381 (2020). https://doi.org/10.1016/j.solmat.2019.110381

11 T.M. Razykov, K.M. Kuchkarov, B.A. Ergashev, Lukas Schmidt-Mende, Tim Mayer, M. Tivanov, M. Makhmudov, D.Z. Isakov, R. Khurramov, M. Primmatov, K.F. Shakhriev, Sh..B.. Utamuradova, R.T. Yuldoshov, Growth and characterization of $Sb_2(S_xSe_{1-x})_3$thin films prepared by chemical-molecular beam deposition for solar cell applications. Thin Solid Films **807**, 140554 (2024). https://doi.org/10.1016/j.tsf.2024.140554

12 TM Razykov KM Kuchkarov MS Tivanov LS Lyashenko DZ Isakov RR Khurramov Z Makhmudov AN Olimov M Pirimmetov PA Sivtsova RT Yuldoshov L Schmidt-Mende KF Shakhriev ShB Utamuradova JG Bekmirzoyev 2024 Effect of substrate temperature on the microstructural and optical properties of chemical molecular beam deposited Sb_2S_3 films J Mater Sci: Mater. Electron. 35 2295 https://doi.org/10.1007/s10854-024-13999-y

13 T.Y. Ko, K.W. Sun, Optical and electrical properties of single Sb_2Se_3nanorod. J. Lumin. **129**(12), 1747–1749 (2009).

14 B. Xu, Y. Du, G. Wang, W. Xiong, Z. Kong, X. Zhao, Y. Miao, Y. Wang, H. Lin, J. Su, B. Li, H.H. Radamson, Dual-step selective homoepitaxy of Ge with low defect density and modulated strain based on optimized Ge/Si virtual

substrate. Materials **15**(10), 3594 (2022). https://doi.org/10.3390/ma15103594

15 H.H. Radamson, A. Hallén, I. Sychugov, A. Azarov, X-ray techniques, in analytical methods and instruments for micro- and nanomaterials, lecture *notes in nanoscale science and technology, vol. 23*. (Springer, Cham, 2023). https://doi.org/10.1007/978-3-031-26434-4_1

16 K. Li, R. Tang, Ch.. Zhu, T. Chen, Critical review on crystal orientation engineering of antimony chalcogenide thin film for solar cell applications. Adv. Sci. , 2304963 (2023). https://doi.org/10.1002/advs.202304963

17 V. Mote, Y. Purushotham, B. Dole, Williamson-Hall analysis in estimation of lattice strain in nanometer-sized ZnO particles. J. Theor. Appl. Phys. (2012). https://doi.org/10.1186/2251-7235-6-6

18 K Patel A Patel VP Jethwa H Patel GK Solanki 2024 X-ray diffraction analysis of orthorhombic SnSe nanopar-ticles by Williamson-Hall, Halder-Wagner and Size-Strain plot methods Chem. Phys. Imp. 8 100547

19 N. Fleck, T.D.C. Hobson, C.N. Savory, J. Buckeridge, T.D. Veal, M.R. Correia, D.O. Scanlon, K. Durosea, F. Jackel, Identifying Raman modes of Sb_2Se_3 and their symmetries using angle-resolved polarised Raman spectra. J. Mater. Chem. A **8**, 8337–8344 (2020). https://doi.org/10.1039/d0ta01783c

20 X. Ma, Z. Zhang, X. Wang, S. Wang, F. Xu, Y. Qian, Large-scale growth of wire-like Sb_2Se_3 microcrystallines via PEG-400 polymer chain-assisted route. J. Cryst. Growth **263**, 491–497 (2004). https://doi.org/10.1016/j.jcrysgro.2003.11.004

21 A. Shongalova, M.R. Correia, B. Vermang, J.M.V. Cunha, P.M.P. Salomé, P.A. Fernandes, On the identification of Sb_2Se_3 using Raman scattering. MRS Commun. **8**(3), 865–870 (2018). https://doi.org/10.1557/mrc.2018.94

22 A. Kumar, V. Kumar, A. Romeo, Raman spectroscopy and in situ XRD probing of the thermal decomposition of Sb_2Se_3 thin films. J. Phys. Chem. C **125**(36), 19858–19865 (2021). https://doi.org/10.1021/acs.jpcc.1c05047

23 R.X. Liu, J. Chen, M. Luo, M. Leng, Z. Xia, Y. Zhou, S. Qin, D.-J. Xue, L. Lv, H. Huang, D. Niu, J. Tang, Thermal evaporation and characterization of Sb_2Se_3 thin film for substrate Sb_2Se_3/CdS solar cells. ACS Appl. Mater. Interfaces **6**, 10687–10695 (2014). https://doi.org/10.1021/am502427s

24 R.Y. Zhang, G. Li, B. Zhang, L. Zhang, Synthesis and characterization of hollow Sb_2Se_3 nanospheres. Mater. Lett. **58**, 2279–2282 (2004). https://doi.org/10.1016/j.matlet.2004.02.006

25 R.Y. Zhou, M. Leng, Z. Xia, J. Zhong, H. Song, X. Liu, B. Yang, J. Zhang, J. Chen, K. Zhou, J. Han, Y. Cheng, J. Tang, Solution-processed antimony selenide heterojunction solar cells. Adv. Energy Mater. **4**, 1301846 (2014). https://doi.org/10.1002/aenm.201301846

26 C.L. David, H.L. Jacob, On the accurate determination of absorption coefficient from reflectance and transmittance measurements: application to Fe-doped GaN. J. Vac. Sci. Technol. B. **34**, 04J105 (2016). https://doi.org/10.1116/1.4954211

27 K. Yang, B. Li, G. Zeng, Effects of substrate temperature and SnO_2 high resistive layer on Sb_2Se_3 thin film solar cells prepared by pulsed laser deposition. Sol. Energy Mater. Sol. Cells. **208**, 110381 (2020). https://doi.org/10.1016/j.solmat.2019.110381

28 W. Chen, Y. Li, Y. Zhou, C. Chen, M. Luo, X. Liu, K. Zeng, B. Yang, C. Zhang, J. Han, J. Tang, Optical properties of amorphous and polycrystalline Sb_2Se_3 thin films prepared by thermal evaporation. Appl. Phys. Lett. **107**, 043905 (2015). https://doi.org/10.1063/1.4927741

29 C. Savory, D. Scanlon, The complex defect chemistry of antimony selenide. J. Mater. Chem. A (2019). https://doi.org/10.1039/C9TA02022E

30 U. Wijesinghe, G. Longo, O.S. Hutter, Defect engineering in antimony selenide thin film solar cells. Energy Adv. (2022). https://doi.org/10.1039/d2ya00232a

31 A. Stoliaroff, A. Lecomte, S. Jobic, X. Zhang, C. Latouche, X. Rocquefelte, Deciphering the role of key defects in Sb_2Se_3, a promising candidate for chalcogenide based solar cells. ACS Appl. Energy Mater. (2020). https://doi.org/10.1021/acsaem.9b02192